Single-sided Bragg reflection waveguides with multilayer core for monolithic semiconductor parametric devices

Payam Abolghasem and Amr S. Helmy*

The Edward S. Rogers Sr. Department of Electrical and Computer Engineering and the Institute of Optical Sciences, University of Toronto, Toronto, Ontario M5S 3G4, Canada
**Corresponding author: a.helmy@utoronto.ca*

Received October 31, 2011; revised February 28, 2012; accepted March 9, 2012;
posted March 12, 2012 (Doc. ID 157367); published May 23, 2012

We propose and examine single-stack matching-layer enhanced Bragg reflection waveguides (BRWs) as a platform for integrated parametric devices. The proposed designed is asymmetric in geometry, where a multilayer core is surrounded by a single-layer upper cladding and a lower quarter-wave Bragg mirror. The propagation of the Bragg mode in the new design relies on total internal reflection from the upper cladding and Bragg reflection from the lower periodic cladding. Analytical expressions for modal analysis of TE- and TM-polarized Bragg modes are derived. An $Al_xGa_{1-x}As$ second-harmonic generation device is theoretically examined to highlight nonlinear performance of the new design, and it is compared to symmetric phase-matched BRWs reported to date. The application of the same structure for generation of anticorrelated photon pairs is discussed.

OCIS codes: 230.7370, 230.1480, 190.2620, 320.7110.

1. INTRODUCTION

Bragg reflection waveguides (BRWs) have been recently proven as a promising platform for exact phase-matching (PM) second-order nonlinear interactions in $Al_xGa_{1-x}As$ [1–3]. Waveguiding in BRWs is achieved through Bragg reflections, which are obtained when the propagating mode properties fall within the photonic stop band of the periodic claddings. In addition, the same structure can be designed to support waveguiding of bound modes formed by total internal reflection (TIR). Using the strong dependence of the photonic bandgap mode dispersion on the structure geometry, BRWs can be designed to attain modal PM between a photonic bandgap mode and bound modes. In addition to applications of on-chip optical frequency mixing, BRWs have been utilized as edge-emitting diode lasers, where the lasing action is predominantly taking place in the BRW mode [4,5]. The availability of an efficient frequency mixing element in addition to an integrated diode laser pump render the BRW structure as an attractive candidate for the implementation of monolithic integrated parametric devices and circuits. Novel photonics components, such as self-pumped difference-frequency generation devices and electrically pumped all-semiconductor optical parametric oscillators, are now feasible through the BRW platform.

To date, three generations of BRW designs have demonstrated PM and frequency conversion. These include conventional quarter-wave BRWs [6,7], matching-layer enhanced BRWs (ML-BRWs) [1] and ML-BRWs with a multilayer core [8]. A common feature in these designs is that the waveguide structure is spatially symmetric with respect to the core, and hence it is surrounded by identical periodic claddings. As such, optical mode confinement in these BRWs is achieved through Bragg reflections at the interfaces of the core and the transverse Bragg reflectors (TBRs). While using identical periodic claddings has been the preferred choice in designing BRWs, there are certain practical impediments in the implementation and utilization of these structures. One major challenge is associated with the thickness of the top cladding, which is also comprised of a significant number of interfaces due to the Bragg stack. These interfaces increase the overall device resistance, impeding the high-power operation of the device through enhanced operating voltage and heating. The overall thickness of the top cladding also impedes the capability of fabricating gratings for distributed feedback lasers and high-Q cavities. It also makes it a challenging task to fabricate good quality ring resonator cavities due to the difficulties in reproducing the in/out couplers to the rings. Another challenge is associated with the coupling efficiency into the Bragg modes from external sources, which would serve as the pump for downconversion processes including difference-frequency generation and spontaneous parametric downconversion (SPDC). Owing to the oscillatory nature of the Bragg mode field profile, conventional coupling techniques, such as free-space coupling and fiber coupling, result in poor spatial overlap factor between the incident pump beam and the excited pump Bragg mode. More involved coupling techniques, such as prism-coupling and grating-coupling [9–11], which require mode excitation from above the sample, are not viable options. This is due to the existence of the upper Bragg reflector, which acts as a high reflector mirror at the pump wavelength, hence prohibiting the transfer of the incident beam energy to the waveguide core.

In addition, a constraint in the implementation of symmetric BRWs is the growth capabilities for the overall thickness of such devices. Using the metal–organic chemical vapor deposition (MOCVD) technique, the overall growth thickness

of the devices is generally limited to ≈8–10 μm to yield good-quality wafers with tolerable defect density. In the near-infrared, this often allows for using between five to seven Bragg reflector pairs on either side of the core, which may not be enough for low substrate leakage loss.

In this work, we introduce the single-sided Bragg reflection waveguide (SS-BRW) as a design, which addresses the aforementioned impediments of BRWs with symmetric periodic claddings. In the proposed structure, the waveguide core is comprised of multiple dielectric layers, which are separated from the substrate by a TBR followed by a matching layer. The top cladding of the device is a single dielectric layer. A schematic of a ridge SS-BRW for integrated parametric devices is shown in Fig. 1. As will be discussed, the efficiency of the second-order nonlinear interactions in SS-BRWs is comparable to those in the previously studied BRWs with symmetric claddings. It should be noted that BRWs with asymmetric claddings have been previously investigated through calculations [12]. In [13], asymmetric BRWs are proposed as single-mode Bragg lasers with high side-mode suppression ratio. In [14], anomalous modal dispersion of asymmetric BRWs in lithium niobate waveguides is reported. Finally, in [15], asymmetric BRWs have been exploited for dispersion control in lithium niobate waveguides to broaden the wavelength tuning bandwidth of optical parametric amplification process. However, they have not been investigated before to provide PM.

The rest of this paper is organized as follows: Section 2 develops the analytical tools required to design and examine the performance of SS-BRWs. Section 3 discusses the design of SS-BRWs for PM and provides an example for the design of a second-harmonic generation device. The same structure is then discussed as an integrated source of photon pairs with frequency anticorrelated properties with applications in quantum communication. Conclusions are then provided in Section 4.

2. MODAL ANALYSIS OF SINGLE-SIDED BRWs

In this section we develop the analytical tools for the design of SS-BRWs. A schematic of a slab SS-BRW is shown in Fig. 2. In this design, the core is a multilayer structure made of dielectric layers with refractive indices $n_a, \ldots, n_l$ with corresponding

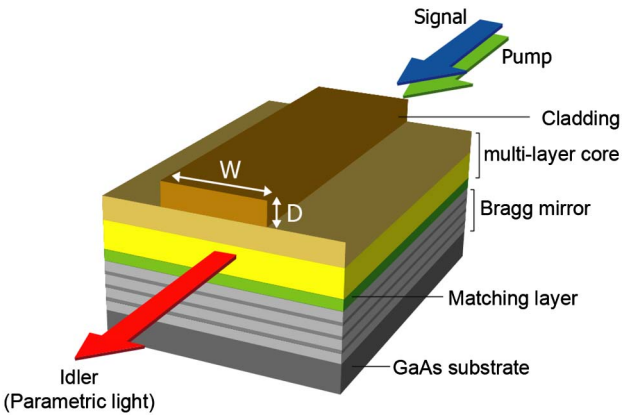

Fig. 1. (Color online) Schematic of a ridge single-stack BRW with ridge width W and etch depth D used for nonlinear three-mixing processes.

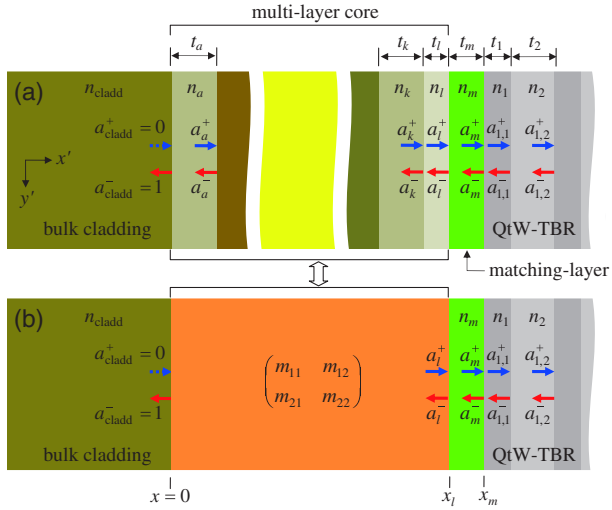

Fig. 2. (Color online) (a) Schematic of a single-stack ML-BRW, where one of the periodic claddings in symmetric BRWs is replaced by a single layer cladding. The matching layer separates the multilayer core composed of dielectric layers with the refractive indices $n_a, n_b, \ldots, n_l$ from the quarter-wave Bragg reflector. (b) Conceptual structure where all the layers between the bulk cladding and the matching layer in (a) are represented by an $ABCD$ matrix with elements $m_{11}, \ldots, m_{22}$. QtW, quarter-wave.

thicknesses of $t_a, \ldots, t_l$. This multilayer core is surrounded on the lower side by a periodic cladding composed of bilayers with refractive indices n_1 and n_2 with associated thicknesses t_1 and t_2. On the upper side of the core, there is a single-layer cladding with a refractive index of n_{cladd} and a thickness of t_{cladd}. A matching layer with an index of n_m and a thickness of t_m separates the periodic cladding from the multilayer core. The purpose of the matching layer in the design of SS-BRW is to tailor the effective mode index of the structure such that the bilayers of the Bragg reflectors satisfy the quarter-wave condition:

$$k_1^x t_1 = (2u+1)\pi/2, k_2^x t_2 = (2v+1)\pi/2, \tag{1}$$

where $u, v = 0, 1, 2, \ldots$. In Eq. (1), k_1^x and k_2^x are the x components of the wave vectors in the bilayers of the periodic cladding. Given the material index of the matching layer, n_m, the ML thickness, t_m, is a parameter with discrete values determined from the dispersion equations. In Fig. 2 a_j^+ and a_j^- are the amplitudes of the right and left propagating fields in the jth layer. The overall field in the jth layer is then formed by the superposition of right and left propagating plane waves with amplitudes a_j^+ and a_j^-. The confinement of the Bragg mode in SS-BRW relies on TIR at $x = 0$, where the bulk cladding is located, and Bragg reflection, at $x = x_m$, from the reflection provided by the Bragg mirror. The TIR at $x = 0$ requires the existence of an evanescent field for $x < 0$, which can be satisfied only if a left propagating plane wave exists in the bulk cladding. As such, the field amplitudes in the bulk cladding are taken as $a_{\text{cladd}}^+ = 0, a_{\text{cladd}}^- = 1$.

Our derivation for the modal dispersion equations relies on the unique field transitions at the interface between the matching layer and the periodic cladding. This field transition simply denotes that for the existence of Bragg reflectors with quarter-wave thick bilayers, the electromagnetic field either

vanishes (node) or peaks (antinode) at the interface where the optical mode extends into the periodic cladding [16]. From Fig. 2, this interface is drawn at $x = x_m$, which is the interface between the ML and the QtW-TBR. In the case of having a node at $x = x_m$, the quarter-wave stack acts as a perfect electric wall, where the tangential component of the electric field vanishes. For the case of having an antinode at $x = x_m$, the quarter-wave stack resembles a perfect magnetic wall where the first-order derivative of the electric field vanishes.

Using the transfer matrix method for the structure in Fig. 2, we relate the right and left propagating field amplitudes of the cladding, $(a^+_{\text{cladd}}, a^-_{\text{cladd}})$, to those of the layer prior to the matching layer (a_l^+ and a_l^-). This relation is expressed as

$$\begin{bmatrix} a_l^+ \\ a_l^- \end{bmatrix} = \begin{bmatrix} m_{11} & m_{12} \\ m_{21} & m_{22} \end{bmatrix} \begin{bmatrix} a^+_{\text{cladd}} \\ a^-_{\text{cladd}} \end{bmatrix}. \tag{2}$$

Using the assumptions that $a^+_{\text{cladd}} = 0$ and $a^-_{\text{cladd}} = 1$, Eq. (2) simplifies to

$$a_l^+ = m_{12}, a_l^- = m_{22}. \tag{3}$$

Given a_l^+ and a_l^-, the field amplitudes in the matching layer, a_m^+ and a_m^-, can be calculated using the single transfer matrix as

$$\begin{bmatrix} a_m^+ \\ a_m^- \end{bmatrix} = \mathbf{T}_m \begin{bmatrix} a_l^+ \\ a_l^- \end{bmatrix}. \tag{4}$$

In Eq. (4), $\mathbf{T}_m$ is the forward transfer matrix of the matching layer, which is defined as

$$\mathbf{T}_m = \frac{1}{2}\begin{bmatrix} (1+f_{\text{P}})\exp(-i\phi_m) & (1-f_{\text{P}})\exp(-i\phi) \\ (1-f_{\text{P}})\exp(+i\phi_m) & (1-f_{\text{P}})\exp(+i\phi_m) \end{bmatrix}, \tag{5}$$

where $\text{P} = \{\text{TE}, \text{TM}\}$ is the subscript used for indicating the polarization state of the propagating field, $\phi_m = k_m^x t_m$ is the phase accumulated in the matching layer, and

$$f_{\text{P}} = \begin{cases} \dfrac{k_l^x}{k_m^x} & \text{for TE polarization} \\ \dfrac{n_m^2 k_l^x}{n_l^2 k_m^x} & \text{for TM polarization} \end{cases}. \tag{6}$$

The field amplitudes in the matching layer can then be calculated using Eq. (4) as

$$a_m^+ = \frac{1}{2}[(m_{12}+m_{22}) + (m_{12}-m_{22})f_{\text{P}}]\exp(-i\phi_m), \tag{7a}$$

$$a_m^- = \frac{1}{2}[(m_{12}+m_{22}) - (m_{12}-m_{22})f_{\text{P}}]\exp(+i\phi_m). \tag{7b}$$

For each orthogonal polarization, the dispersion relation can be derived by forcing the overall field at $x = x_m$ to be either zero ($a_m^+ + a_m^- = 0$) or maximum ($a_m^+ - a_m^- = 0$). From Eqs. (7) for TE-polarization, the electric field vanishes at $x = x_m$ when $k_m^x < k_1^x$ and it peaks when $k_m^x > k_1^x$. Using (7), the dispersion relation of TE-propagating mode is obtained as

$$\begin{aligned} \cot(k_m^x t_m) &= +if_{\text{TE}}\frac{m_{12}-m_{22}}{m_{11}+m_{22}} \quad (k_m^x < k_1^x) \\ \tan(k_m^x t_m) &= -if_{\text{TE}}\frac{m_{12}-m_{22}}{m_{11}+m_{22}} \quad (k_m^x > k_1^x) \end{aligned}. \tag{8}$$

Equations (8) can be solved to calculate the required thicknesses of the matching layer as

$$\begin{aligned} t_m &= \tfrac{1}{k_m^x}\left[\text{acot}\left(+if_{\text{TE}}\frac{m_{12}-m_{22}}{m_{12}+m_{22}}\right)+p\pi\right] \quad (k_m^x < k_1^x) \\ t_m &= \tfrac{1}{k_m^x}\left[\text{atan}\left(-if_{\text{TE}}\frac{m_{12}-m_{22}}{m_{12}+m_{22}}\right)+p\pi\right] \quad (k_m^x > k_1^x) \end{aligned}. \tag{9}$$

Similarly, for a propagating mode with a TM polarization state, the field vanished at $x = x_m$ when $n_1^2 k_m^x < n_m^2 k_1^x$ and it peaks when $n_1^2 k_m^x > n_m^2 k_1^x$. Using Eq. (7), the dispersion relation of TM-propagating mode is obtained as

$$\begin{aligned} \cot(k_m^x t_m) &= +if_{\text{TE}}\frac{m_{12}-m_{22}}{m_{11}+m_{22}} \quad (n_1^2 k_m^x < n_m^2 k_1^x) \\ \tan(k_m^x t_m) &= -if_{\text{TM}}\frac{m_{12}-m_{22}}{m_{12}+m_{22}} \quad (n_1^2 k_m^x > n_m^2 k_1^x) \end{aligned}, \tag{10}$$

with the matching layer thickness given by

$$\begin{aligned} t_m &= \frac{1}{k_m^x}\left[\text{acot}\left(+if_{\text{TM}}\frac{m_{12}-m_{22}}{m_{12}+m_{22}}\right)+p\pi\right] \quad (n_1^2 k_m^x < n_m^2 k_1^x) \\ t_m &= \frac{1}{k_m^x}\left[\text{atan}\left(-if_{\text{TM}}\frac{m_{12}-m_{22}}{m_{12}+m_{22}}\right)+p\pi\right] \quad (n_1^2 k_m^x > n_m^2 k_1^x) \end{aligned}. \tag{11}$$

Equations (8)–(11) are the design equations of the single-stack BRWs. In the next section, we use these equations for the design of phase-matched SS-BRWs for second-order nonlinear interactions in AlGaAs waveguides.

3. PHASE MATCHING USING SINGLE-STACK BRW

The large number of parameters, including the refractive indices and thicknesses of the layers, defines a large parameter space to span for the design of SS-BRWs. As such, a systematic search of this parameter space is not an effective route to use for the design of these structures. Typical SS-BRWs are composed of many layers in the range of a few tens. Design optimization of such structures can be carried out using any one of the numerous optimization techniques. The following procedure describes the technique we adopted for designing phase-matched SS-BRWs:

1. For a given nonlinear interaction, determine the type of the optical modes (Bragg mode or TIR mode) and their polarizations involved in the frequency-mixing process.
2. Choose the materials of the multilayer core, $n_a, \ldots, n_l$; the cladding, n_{cladd}; the bilayers of the Bragg reflectors, n_1 and n_2; and the matching layer, n_m—considering material constraints such as linear/nonlinear absorption and oxidation.
3. Choose the thicknesses of the layers of the complex core, $t_a, \ldots, t_l$ and the cladding thickness, t_{cladd}.
4. Given the refractive index profile of the structure at each wavelength involved in the nonlinear interaction, determine the range of the effective mode indices $[n_{\text{eff},1}, n_{\text{eff},2}]$ within which the PM condition might be satisfied.
5. For $n_{\text{eff}} \in [n_{\text{eff},1}, n_{\text{eff},2}]$, given the polarization of the Bragg mode, calculate the matching layer thickness, t_m, using Eq. (9) or (11).

6. Using the quarter-wave condition of Eq. (1), determine the thicknesses of the Bragg reflector bilayers, t_1 and t_2.

7. Given the number of periods of bilayers within the Bragg reflector, construct the structure using $(n_{\text{cladd}}, n_a, \ldots, n_l, n_m, n_1, n_2)$ and $(t_{\text{cladd}}, t_a, \ldots, t_l, t_m, t_1, t_2)$.

8. Solve for TE- and TM-polarized TIR modes for the wavelengths propagating as bound modes.

9. Given the dispersion of Bragg and TIR modes as functions of n_{eff}, determine the value of n_{eff} for which the PM condition is satisfied.

10. Determine the nonlinear properties of the design, including nonlinear overlap factor, nonlinear conversion efficiency, and structure effective second-order nonlinearity.

11. Use perturbations in the waveguide parameters and go to step 1 to determine a locally optimum design.

12. Using a 2D mode solver, investigate the effect of the waveguide ridge width and depth on the nonlinear properties such as the detuning of the PM wavelength from that of the 1D case.

Two case studies employing the aforementioned procedure will be given. Next we discuss the design of a SHG device for frequency doubling within the C-band telecommunication wavelength and the same design as an integrated source of frequency anticorrelated photon pairs generated via SPDC.

A. Second-Harmonic Generation Using the Single-Stack BRW

Consider a Type II SHG process where a pump at frequency ω with hybrid TE + TM polarization state generates a TE-polarized second harmonic at 2ω. The PM condition for this process is expressed as $n_{\text{eff},2\omega}^{(\text{TE})} = 1/2\left[n_{\text{eff},\omega}^{(\text{TE})} + n_{\text{eff},\omega}^{(\text{TE})}\right]$ where $n_{\text{eff},\omega}^{(\text{TE})}$ and $n_{\text{eff},\omega}^{(\text{TM})}$ are the effective mode indices of TE- and TM-polarized pump, respectively, and $n_{\text{eff},2\omega}^{(\text{TE})}$ is the mode index of the TE-polarized SH.

Using $Al_xGa_{1-x}As$ as the material system, we simulated a series of SS-BRWs for Type II SHG with a pump at 1540 nm frequency doubled to a SH signal at 740 nm. In this design, the element with lowest aluminum fraction is limited to be $Al_{0.20}Ga_{0.80}As$ to avoid two-photon absorption of the pump, and that with the highest aluminum content is limited to be $Al_{0.85}Ga_{0.15}As$ to avoid excessive oxidation. This choice for the $Al_xGa_{1-x}As$ elements was identical to that of the single-layer core ML-BRW, which has so far been demonstrated to have the highest SHG conversion efficiency in BRW devices [1]. Using initial simulations to determine a locally optimum structure, the core of the simulated SS-BRWs consisted of two layers of $Al_{0.20}Ga_{0.80}As/Al_{0.48}Ga_{0.52}As$ with respective thicknesses of 210 nm/310 nm. The bottom TBR consisted of six periods of bilayers $Al_{0.20}Ga_{0.80}As/Al_{0.70}Ga_{0.30}As$. The upper cladding was $Al_{0.85}Ga_{0.15}As$ with a thickness of 500 nm. To obtain the phase-matched structure, we swept the effective index, n_{eff}, in the range of $[n_{\text{neff},1}, n_{\text{neff},2}] = [3.100\ 3.175]$ within which the PM condition could be satisfied. The choice of $n_{\text{eff},1}$ was such that the optical modes of the pump and SH be evanescent within the upper cladding layer. This condition could be satisfied when

$$n_{\text{eff},1} > n_{\text{cladd},2\omega} > n_{\text{cladd},\omega}, \tag{12}$$

where $n_{\text{cladd},\omega} = 2.9549$ and $n_{\text{cladd},2\omega} = 3.0942$ were obtained using the Gehrsitz model [17] for $Al_{0.85}Ga_{0.15}As$ cladding.

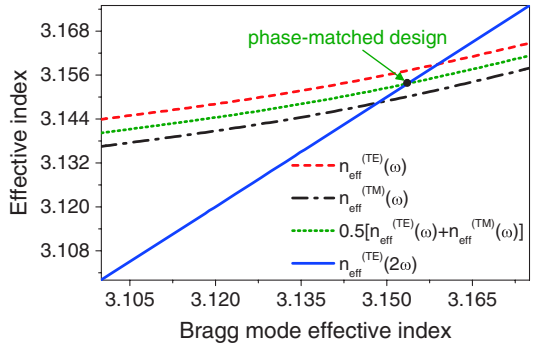

Fig. 3. (Color online) Variation of effective mode indices of TE- and TM-polarized pump and TE-polarized second harmonic as functions of the Bragg mode effective index in BRW_{III} designed for Type II PM.

The choice of $n_{\text{eff},2}$ was such that the leaky mode condition at the second-harmonic wavelength could be satisfied by

$$n_{\text{eff},2} < \min\{n_a, n_b, n_m, n_1, n_2\}_{2\omega}, \tag{13}$$

where $(n_a, n_b)_{2\omega} = (3.5381, 3.3160)$ are the refractive indices of the layers composing the waveguide core, $n_{m,2\omega} = 3.5381$ is the refractive index of the matching layer, and $(n_1, n_2)_{2\omega} = (3.1801, 3.5381)$ are the refractive indices of the bilayers of the Bragg mirrors. Having the effective index range defined by $[n_{\text{neff},1}, n_{\text{eff},2}]$, we sweep n_{eff} within this range as the mode index of TE-polarized Bragg mode and construct the associated SS-BRW using the algorithm discussed earlier. The structure is then solved for the bound modes of TE and TM polarizations of the pump at 1540 nm. The dependence of the mode indices of the pump and SH signal on n_{eff} is shown in Fig. 3. From the figure, the dotted curve denotes the variation of $1/2\left[n_{\text{eff},\omega}^{(\text{TE})} + n_{\text{eff},\omega}^{(\text{TM})}\right]$ as a function of n_{eff}. The crossing of this curve with the graph of $n_{\text{eff},2\omega}^{(\text{TE})}$ determines the design, referred to as BRW_{III}, for which the Type II PM condition is satisfied. A summary of BRW_{III} is provided in Table 1.

Figure 4(a) illustrates the index profiles of BRW_{III} at the pump (dashed line) and the second-harmonic (solid line) frequencies. In the figure, the dashed line denotes effective mode index of the TE-polarized second harmonic at PM. Also, shown in Fig. 4(b) are the field profiles of the interacting modes in BRW_{III}. The second-harmonic mode in BRW_{III} is hybrid in nature in the sense that it undergoes TIR at the boundary of the multilayer core with the bulk cladding while it experiences Bragg reflection at the interface between the matching layer and the Bragg reflector. From Fig. 4(b), this can be observed by noticing that the field profile of the SH

Table 1. Summary of the BRW_{III} Structure Phase Matched for Type II Second-Harmonic Generation with a Pump at 1540 nm

Parameter	Value
$(t_{\text{cladd}}, n_{\text{cladd}}, n_{\text{cladd},2\omega})$	(500 nm, 2.9549, 3.0942)
$(t_a, n_{a,\omega}, n_{a,2\omega})$	(210 nm, 3.2656, 3.5381)
$(t_b, n_{b,\omega}, n_{b,2\omega})$	(310 nm, 3.1279, 3.3160)
$(t_m, n_{m,\omega}, n_{m,2\omega})$	(358 nm, 3.2656, 3.5381)
$(t_1, n_{1,\omega}, n_{1,2\omega})$	(481 nm, 3.0227, 3.1801)
$(t_2, n_{2,\omega}, n_{2,2\omega})$	(120 nm, 3.2656, 3.5381)

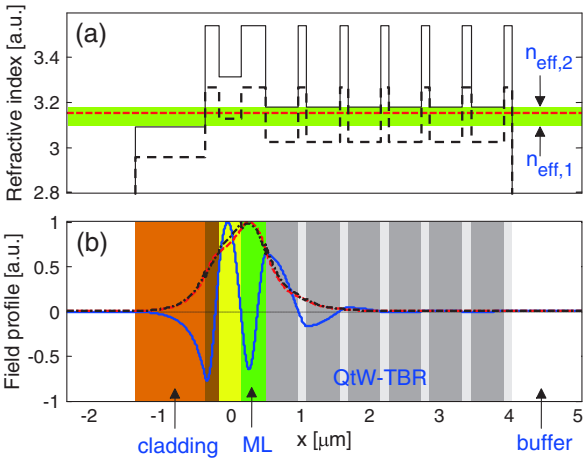

Fig. 4. (Color online) (a) Index profile of BRW_{III} at the second-harmonic wavelength (solid curve) and that at pump wavelength (dashed curve). The horizontal dashed line indicates PM effective index effective index for Type II SHG. (b) Field profile of TE-polarized pump (dashed curve), TM-polarized pump (dashed–dotted curve) and TE-polarized SH (solid line).

(solid curve) is evanescent within the bulk cladding while it is oscillatory within the QtW-TBR.

BRWs have the remarkable feature that the modal birefringence between the orthogonal polarizations, defined as $\Delta n = n_{\text{eff}}^{(\text{TE})} - n_{\text{eff}}^{(\text{TM})}$, is generally very small. A special case is quarter-wave BRWs without a matching layer, which are polarization degenerate with $\Delta n = 0$. For the phase-matched BRW, the small modal birefringence is attractive, as it enables a different modality of PM to take place within a narrow spectral window. For example, in [18], it is demonstrated that a ML-BRW with symmetric claddings can support three distinct PM types, namely Type 0 ($\text{TM}_\omega \rightarrow \text{TM}_{2\omega}$), Type I ($\text{TE}_\omega \rightarrow \text{TM}_{2\omega}$), and Type II ($\text{TE}_\omega + \text{TM}_\omega \rightarrow \text{TE}_{2\omega}$), within a spectral window as narrow as 17 nm. A recent theoretical investigation has shown that the small birefringence in BRWs is significant for applications in quantum optics where hyperentangled photon pairs are generated through SPDC [19]. As such, it is worth investigating the modal birefringence in SS-BRWs proposed here. In Fig. 5(a), we have plotted the effective mode indices of the TE- and TM-polarized pump and those of the second harmonic for the pump wavelength in the range of 1530–1550 nm in BRW_{III}. In the figure, the crossing points denoted as P_1, P_2, and P_3 indicate the pump wavelengths for which the PM condition are satisfied. Point P_1 with a pump wavelength around 1531 nm denotes a Type I SHG, point P_2 is the Type II design of BRW_{III} with the pump wavelength at 1540 nm, and point P_3 is associated with a Type 0 SHG with a pump wavelength around 1543 nm. In this case, the wavelength separation between Type I and Type 0 SHG in BRW_{III} is only 9 nm. Also in Fig. 5, we have plotted the modal birefringence of the SH Bragg mode and the pump bound mode for comparison. As expected, the SH Bragg mode inherits smaller modal birefringence in comparison to that of the pump mode.

In order to highlight the nonlinear performance of BRW_{III}, we theoretically compare its salient nonlinear parameters with those previously reported in symmetric BRWs including the single-layer core ML-BRW in [1], referred to as BRW_I, and the multilayer core device in [8], referred to as BRW_{II}. The comparison with BRW_I is particularly attractive because it

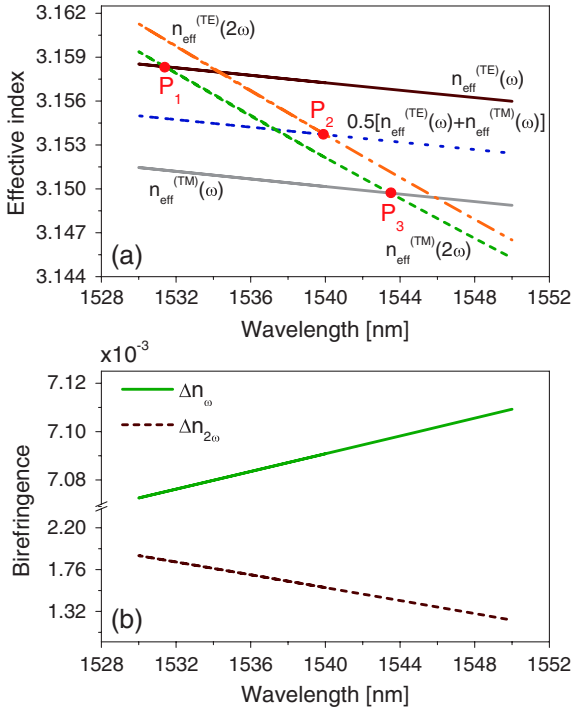

Fig. 5. (Color online) (a) Variations of effective mode indices of orthogonal polarizations of TE- and TM-polarized pump mode and those of the second-harmonic mode in BRW_{III} design. The crossing points at P_1, P_2, and P_3 denote the pump wavelengths for Type I, Type II, and Type 0 PM, respectively. (b) Dependency of modal birefringence of the pump and second harmonic on pump wavelength in BRW_{III}.

is a structure with the highest reported conversion efficiency in BRW structures for SHG. Table 2 compares the various parameters including PM wavelength, λ_p; spatial nonlinear overlap factor, ξ; effective second-order nonlinear coefficient, d_{eff}; and normalized nonlinear conversion efficiency, $\bar{\eta}_{\text{SHG}}$ [8]. A comprehensive examination of BRW_I and BRW_{II} can be found in [1] and [8], respectively. From Table 2, it can be seen that the single-stack structure of BRW_{III} benefits from an enhanced nonlinear interaction by ≈67%. This is remarkable because BRW_I has been demonstrated as the most efficient SHG device in this platform [1]. The key point in improving the conversion efficiency in SS-BRWs, resides in the hybrid nature of the Bragg mode where its profile is oscillatory with exponential decay in the lower periodic cladding and it is evanescent in the single-layer upper cladding. In symmetric BRWs, the oscillatory nature of the Bragg mode within both periodic claddings results in poor spatial overlap between the Bragg mode and the bound modes involved in the nonlinear interaction. However, in SS-BRW, the evanescent field in the upper

Table 2. Simulated Nonlinear Parameters of BRW_I, BRW_{II}, and BRW_{III} for Type II Second-Harmonic Generation

Design	λ_p [nm]	ξ $[\text{m}]^{-1}$	d_{eff} [pm/V]	$\bar{\eta}$SHG $[\%\text{W}^{-1}\,\text{cm}^{-2}]$
BRW_I[a]	1546.5	221	40	3.0×10^{-4}
BRW_{II}[b]	1540.0	133	38	1.1×10^{-4}
BRW_{III}	1540.0	196	57	5.0×10^{-4}

[a]See [1].
[b]See [8].

cladding without field oscillation improves the spatial overlap factor between the Bragg mode and the bound modes, which are also evanescent in the upper cladding. It should be mentioned that our choice of a two-layer core in BRW_{III} was only an example to illustrate the proposed design. In practice, the number of layers composing the core, their material contents and thicknesses can be exploited as design parameters to alleviate PM and also to improve the device nonlinear performance.

A merit in studying the performance of an on-chip parametric device is the propagation loss of the optical modes, which is associated with the absorption loss, the scattering loss, and the substrate leakage. Linear absorption in $Al_xGa_{1-x}Gas$ devices is generally avoided by choosing elements with bandgap energies above the highest photon energy involved in the parametric process [20]. For all designs discussed here, the choice of $Al_xGa_{1-x}Gas$ elements is such that linear absorption is negligible. Scattering loss originating from rough waveguide sidewalls forms the major form of optical loss and is related to the quality of waveguide patterning through lithography and plasma etching. Previously reported results indicate that typical scattering loss in BRWs is in the range of 2.0–2.2 cm^{-1} for the pump and in the range of 41–47 cm^{-1} for the second harmonic, which can be further reduced by enhancing the quality of the etch for fabricating the ridges [1]. Leakage loss in symmetric BRWs as well as SS-BRWs is negligible. To show this, we examined the leakage loss coefficient, which is defined as

$$\alpha_{\mathrm{leak},\omega_\sigma}^{(\mathrm{TE/TM})} = 4\pi\kappa_{\mathrm{leak}}^{(\mathrm{TE/TM})}/\lambda_{\omega_\sigma}, \tag{14}$$

where $\omega_\sigma \in \{\omega, 2\omega\}$ and $\kappa_{\omega_\sigma}^{(\mathrm{TE/TM})}$ is the imaginary part of the effective mode index [21]. Figures. 6(a) and 6(b) illustrate the dependence of leakage loss coefficient of pump and second harmonic in BRW_{III} on the aluminum concentration of the buffer, respectively. In Fig. 6(a), TE- and TM-polarized pump modes exhibit leakage loss for buffer Al concentrations less than $x = 0.41\%$ and 0.43%, respectively, where the real part of the effective mode indices lies below the material index of the substrate. For a buffer Al fraction above these values, the pump mode transforms into a bound mode with a pure real effective mode index. From Fig. 6(b), the leakage loss coefficients of TE- and TM-polarized second-harmonic modes are approximately 3 orders of magnitude higher than those of the pump. In comparison to TE polarization, TM-polarized SH seems to suffer from more losses due to the normal configuration of the electric field. Overall, for both pump and SH modes, the dominant loss mechanism is attributed to scattering losses.

In terms of device fabrication, the advantages of SS-BRW in comparison to the symmetric structures is threefold. First, for BRW_I and BRW_{II}, the overall wafer thicknesses were ≈8.6 μm [1] and ≈8.9 μm [8], respectively, while for BRW_{III} the growth thickness is limited to ≈5.0 μm. Using MOCVD as a growth technique, this reduction in the thickness of the single-stack structure facilitates the yield of high-quality wafers with reduced wafer defects. Second, using fabrication technologies, such as molecular beam epitaxy, which allow the growth of thick structures, the BRW_{III} benefits from the possibility of adding more periods of bilayers to the bottom TBR, which helps reduce the substrate leakage. Third, as the field in the upper bulk cladding of single-stack BRWs is evanescent, its thickness can be restricted to a few hundreds of nanometers. In BRW_{III}, the top cladding has a thickness of 500 nm. In the symmetric structures of BRW_I and BRW_{II}, the periodic upper cladding had a thickness of ≈3.5 μm and ≈3.1 μm, respectively. Patterning ridge waveguides with good-quality, smooth ring structures and periodic gratings for cavities and distributed Bragg reflection lasers is more challenging for a deep etch depth. The small thickness of the upper cladding in BRW_{III} is beneficial for reducing the etch depth hence enhancing the quality of the devices.

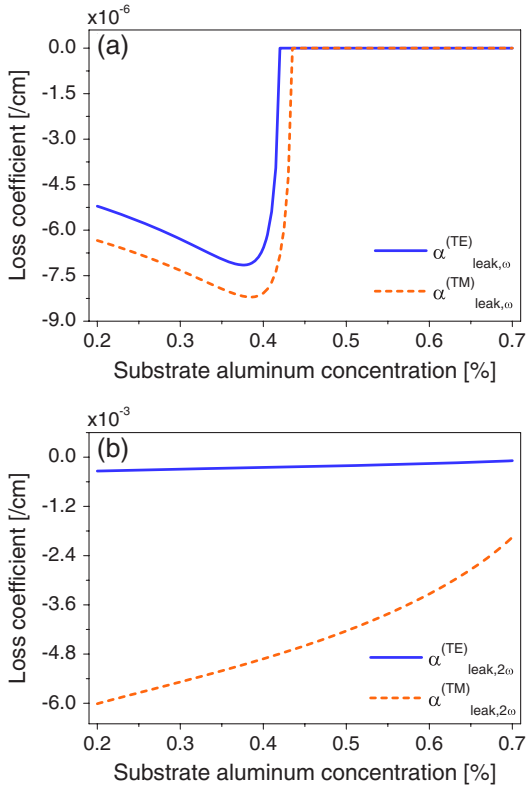

Fig. 6. (Color online) Simulated leakage loss as a function of substrate aluminum concentration in BRW_{III} of (a) TE- and TM-polarized pump mode and (b) those of the second-harmonic mode.

The existence of an evanescent field in the upper cladding of the SS-BRW is additionally beneficial for device operation. For example, DFG devices based on BRWs require excitation of the Bragg mode as the pump. Conventional coupling techniques, such as end-fire coupling, are generally inefficient approaches for this purpose, owing to the poor spatial overlap factor between an incident Gaussian beam and the Bragg mode. The existence of the evanescent field within the upper cladding of SS-BRWs allows the investigation of efficient coupling techniques, particularly grating-assisted coupling. Investigation of integrated grating couplers has been extensively carried out in semiconductor waveguides and is not the focus of this paper [9–11]. However, an important waveguide parameter that is closely related to the design of a grating coupler and waveguide nonlinear properties is the thickness of the upper cladding, t_{cladd}. For this purpose, we examined the dependency of $\bar{\eta}_{\mathrm{SHG}}$ and ξ on t_{cladd} in BRW_{III} for thicknesses in the range of 0.5–2 μm. The result is illustrated in Fig. 7, where both $\bar{\eta}_{\mathrm{SHG}}$ and ξ decrease as t_{cladd} increases. The rate of change

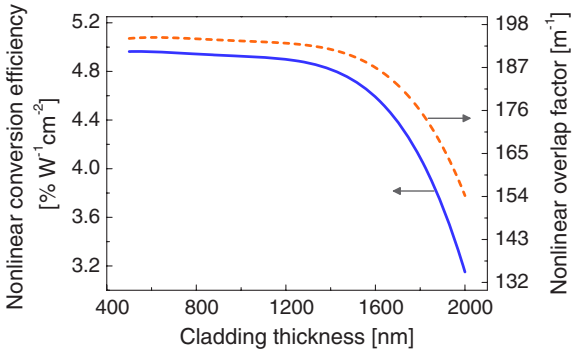

Fig. 7. (Color online) Dependence of normalized conversion efficiency, $\bar{\eta}$SHG, and nonlinear modal overlap, ξ, on the thickness of top cladding in single-stack BRW$_{III}$.

of $\bar{\eta}_{SHG}$ and ξ with respect to t_{cladd} is small for cladding thicknesses less than 1200 nm. This behavior was understood by the fact that in the simulations, the outermost medium was taken as air to resemble an experimental arrangement. A thin t_{cladd} resulted in the close proximity of the optical modes with the surrounding air. Because of the large index contrast between the optical mode indices and air, optical confinement was enhanced with thin t_{cladd} in comparison to designs with thick upper cladding.

Comparing dispersion properties of the three discussed designs is also informative. Dispersion engineering in BRWs has been an important topic in these structures to understand the effect of modal dispersion on nonlinear parameters, including the PM bandwidth and effective interaction length. The group velocity mismatch (GVM) between two frequencies involved in a $\chi^{(2)}$ process is an important merit. For example, in applications involving ultrashort pulses, group velocity mismatch results in temporal pulse walk-off between two interacting frequencies which degrades the efficiency of the interaction. The group velocity mismatch between, for example, the TM-polarized pump and TE-polarized second-harmonic is expressed as

$$\mathrm{GVM}_{2\omega,\omega}^{(\mathrm{TE,TM})} = \frac{1}{v_{g,2\omega}^{(\mathrm{TE})}} - \frac{1}{v_{g,\omega}^{(\mathrm{TM})}}, \tag{15}$$

where $v_{g,\omega}^{(\mathrm{TM})}$ and $v_{g,2\omega}^{(\mathrm{TE})}$ are the group velocities of the pump and SH modes, respectively. Group velocity dispersion (GVD) is also an important parameter for applications involving ultrashort pulses. Certain waveguide designs require minimal GVD at the operating wavelength to reduce the pulse distortion along the propagation distance. For a TE-polarized pump, the GVD, $\mathrm{GVD}_{\omega}^{(\mathrm{TE})}$, is expressed as

$$\mathrm{GVD}_{\omega}^{(\mathrm{TE})} = \frac{\partial^2 \beta_{\omega}^{(\mathrm{TE})}}{\partial \omega^2} = \frac{2}{c}\frac{\partial n_{\mathrm{eff},\omega}^{(\mathrm{TE})}}{\partial \omega} + \frac{\omega}{c}\frac{\partial^2 n_{\mathrm{eff},\omega}^{(\mathrm{TE})}}{\partial \omega^2}. \tag{16}$$

Table 3 summarizes the GVM and GVD of interacting modes for Type II SHG in BRW$_{I}$, BRW$_{II}$, and BRW$_{III}$ designs. From Table 3, the GVM between different harmonics in all three designs is comparable. As expected, the GVM between the orthogonal polarizations of the pump is the lowest due to the fact that the propagation of both TE- and TM-polarized pump modes relies on TIR. For second-order dispersion, in all three designs, the GVD of TE-polarized SH is larger than that of the TE- and TM-polarized pump. Also, it is noticeable that $\mathrm{GVD}_{2\omega}^{(\mathrm{TE})}$ in BRW$_{III}$ is approximately another of magnitude larger than $\mathrm{GVD}_{\omega}^{(\mathrm{TE})}$ and $\mathrm{GVD}_{\omega}^{(\mathrm{TM})}$ in the same structure. It should be noted that first- and second-order dispersion in BRW$_{II}$ is the lowest when compared with BRW$_{I}$ and BRW$_{III}$ devices. This can be attributed to the fact that the structure of BRW$_{II}$ was utilizing $Al_xGa_{1-x}As$ elements with high aluminum fractions, which resulted in reduced material dispersion. Comparing the data in Table 3, one can expect similar dispersion behavior, to the first order, in single-stack BRW as that in BRWs with symmetric periodic cladding while second-order dispersion in single-stack devices appears to be stronger.

B. Photon Pair Generation Using the Single-Stack BRW

The single-stack BRW can be used as an integrated source of photon pairs generated through SPDC for applications in quantum communication and computation. In SPDC using BRWs, the pump mode at the 2ω frequency propagates as a Bragg mode while the pair of downconverted photons propagate as bound modes. BRWs as on-chip sources of photon pairs have been theoretically investigated in some previous works. For example, in [19], BRWs with non-quarter-wave TBRs were studied as a source of biphotons with polarization hyperentanglement property. Also in [22], generation of photon pairs with a frequency anticorrelation property was studied where strong waveguide dispersion in ridge devices was utilized to tailor biphotons spectral bandwidth. Dispersion control using ridge effects in BRWs is a prominent mechanism to attain a desired characteristic of photon pairs. Here, we examine the dispersion properties of ridge SS-BRWs for potential applications in quantum optics. To do so, we consider BRW$_{III}$ as the underlying design and examine its dispersion properties once ridge effects are applied.

Figure 8 illustrates the modal birefringence, Δn, of the pump and downconverted light as a function of ridge width, W, varying between 1.5–5 μm, simulated at PM wavelength associated with each ridge width. From the figure, the crossing points of the birefringence curves with the horizontal dashed line at $\Delta n = 0$ denotes polarization degenerate designs for the pump and photon pairs at which effective indices of TE and TM modes are identical. For the pump frequency, $\Delta n_{2\omega} = 0$ is simulated for a ridge width of ≈2.0 μm while for photon pairs $\Delta n_{\omega} = 0$ for a device with a ridge width of ≈1.6 μm. Also shown in the inset of Fig. 8 is the dependency of the PM

Table 3. Group Velocity Mismatch and Group Velocity Dispersion of the Pump and Second-Harmonic in BRW$_{I}$, BRW$_{II}$, and BRW$_{III}$ for Type II Second-Harmonic Generation

Design	$\mathrm{GVM}_{\omega,\omega}^{(\mathrm{TE,TM})}$ [ps/mm]	$\mathrm{GVM}_{2\omega,\omega}^{(\mathrm{TE,TE})}$ [ps/mm]	$\mathrm{GVM}_{2\omega,\omega}^{(\mathrm{TE,TM})}$ [ps/mm]	$\mathrm{GVD}_{\omega}^{(\mathrm{TE})}$ [fs^2/μm]	$\mathrm{GVD}_{\omega}^{(\mathrm{TM})}$ [fs^2/μm]	$\mathrm{GVD}_{2\omega}^{(\mathrm{TE})}$ [fs^2/μm]
BRW$_{I}$	0.0330	2.4876	2.5206	1.4363	1.4316	5.7712
BRW$_{II}$	0.0101	2.3724	2.3825	1.0436	1.0387	3.4062
BRW$_{III}$	0.0142	3.1208	3.1350	1.2851	1.2757	12.093

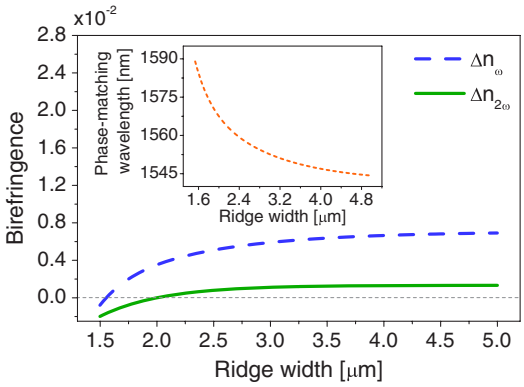

Fig. 8. (Color online) Modal birefringence between the TE and TM modes of downconverted light and that of the pump (dashed line) simulated at associated PM wavelength. For either pump or downconverted wavelengths, there exists a ridge width for which the device is polarization degenerate with vanishing modal birefringence. Inset, dependence of PM wavelength on ridge width in BRW_{III} structure.

wavelength, λ_{PM}, on W where redshift of λ_{PM} is anticipated as W is reduced. For ridge widths greater than ≈3 μm, variation of λ_{PM} on W is less than 10 nm while for $W = 1.5$ μm, the PM wavelength is redshifted by about 52 nm.

The dependence of the GVM between the orthogonal components of the pump and downconverted light on ridge width are shown in Fig. 9(a). From the figure, $GVM_{2\omega,\omega}^{(TE,TE)}$ and $GVM_{2\omega,\omega}^{(TE,TM)}$ are close to each other over the entire range of ridge variation, between 1.5 – 5 μm. However, the GVM between the TE- and TM-polarized downconverted modes is over an order of magnitude smaller than the GVM between the pump and photon pairs. Also shown in Fig. 9 are the GVDs of the TE- and TM-polarized downconverted modes and the TE-polarized pump as functions of ridge width. From the figure, the GVD of the pump is approximately an order of magnitude larger than those of the photon pairs, which matches to the simulated results of the slab case in Table 3.

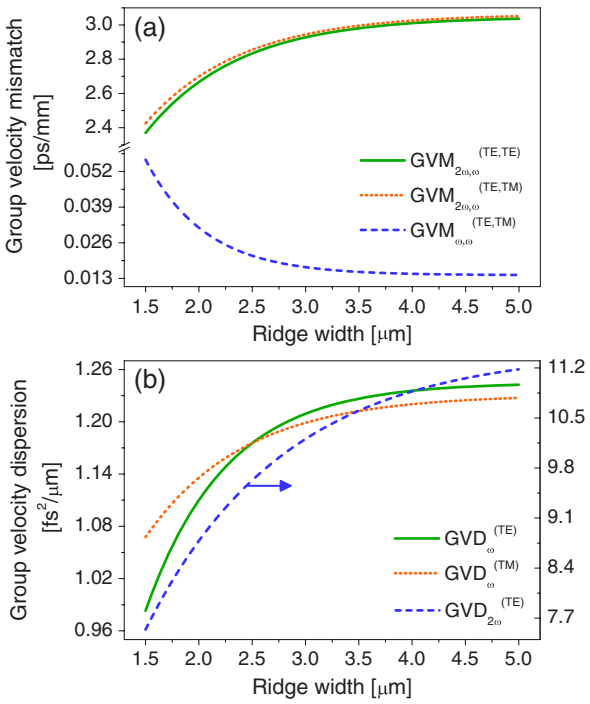

Fig. 9. (Color online) Variations of (a) GVM and (b) GVD in BRW_{III} as functions of ridge width.

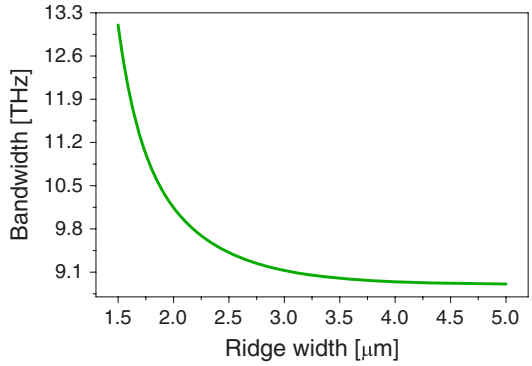

Fig. 10. (Color online) Variation of FWHM spectral bandwidth of anticorrelated photon pairs generated in BRW_{III} as a function of ridge width.

In the generation of anticorrelated photon pairs using Type II SPDC, the spectral bandwidth of the photon pair is determined by the width of the joint power spectral intensity of the biphotons, which in turn is proportional to the $\mathrm{sinc}^2(\Delta\beta L/2)$ function, where $\Delta\beta$ is the SPDC phase mismatch and L is the device length [22]. Using the Taylor series in expanding $\Delta\beta$, one can write

$$\Delta\beta \approx GVM_{\omega,\omega}^{(TE,TM)}\Omega - \frac{1}{2}[GVD_{\omega}^{(TE)} + GVD_{\omega}^{(TM)}]\Omega^2, \qquad (17)$$

where $|\Omega|$ is the magnitude of the angular frequency deviation of the downconverted photons. Using Eq. (17) and the simulated dispersion values presented in Figs. 9(a) and 9(b), we estimated the full-width at half-maximum (FWHM) bandwidth of anticorrelated photon pairs generated in BRW_{III}. The result is shown in Fig. 10, where the FWHM spectral bandwidth of biphotons is plotted as a function of ridge width for a device with a length of $L = 3$ mm From the figure, the spectral bandwidth decreases as the ridge width increases, and it converges to a value of ≈8.9 THz for ridge widths larger than ≈3.5 μm. Maximum bandwidth of ≈13.1 THz is obtained for $W = 1.5$ μm. In [22], Type II SPDC in quarter-wave BRW with symmetric stacks was theoretically studied as on-chip sources of narrowband anticorrelated photon pairs. In that work, a bandwidth of 101 GHz was predicted in a device with a ridge width as small as 375 nm. The smallest SPDC bandwidth of 8.9 THz predicted here is approximately an order of magnitude larger than the work in [22], indicating that the BRW_{III} is not the favored design for the generation of narrowband anticorrelated photon pairs. However, the same structure can be used for the generation of wideband anticorrelated photon pairs in the Type II PM configuration. In comparison to the work in [22], the maximum spectral bandwidth of 61 THz for Type I generated photon pairs was simulated in a ridge BRW with $W = 677$ nm width. In the BRW_{III} proposed here, the spectral bandwidth of 13.1 THz is simulated for $W = 1.5$ μm, which can be further increased using devices with smaller ridge widths and shorter lengths. Considering the ease in fabrication of single-stack BRWs, it is expected that this class of devices can be useful for large SPDC bandwidth control of anticorrelated photon pairs.

4. CONCLUSION

In summary, we studied single-stack matching-layer-enhanced BRWs as a platform for integrated parametric devices. In the proposed structure, the propagation of the Bragg mode is consisted of TIR from an upper single-layer cladding and Bragg reflection from a lower quarter-wave Bragg reflector. The deployment of the matching layer, which separates a multilayer core from the bottom cladding, enabled extracting analytical expressions for the modal analysis of TE- and TM-polarized Bragg modes. Using the proposed design, a SHG device is examined and its performance was predicted to provide nonlinear efficiency at least 1.5 times larger than the previously reported BRWs with symmetric claddings. The existence of an evanescent field with the upper cladding in the SS-BRW makes the examination of preferential coupling techniques including prism coupling and grating coupling feasible in BRW technology.

ACKNOWLEDGMENT

We gratefully acknowledge the support of the Natural Sciences and Engineering Research Council of Canada (NSERC) for funding this research.

REFERENCES

1. P. Abolghasem, J. Han, B. J. Bijlani, A. Arjmand, and A. S. Helmy, "Highly efficient second-harmonic generation in monolithic matching layer enhanced $Al_xGa_{1-x}As$ Bragg reflection waveguides," IEEE Photon. Technol. Lett. **21**, 1462–1464 (2009).
2. J. Han, P. Abolghasem, B. J. Bijlani, and A. S. Helmy, "Continuous-wave sum-frequency generation in AlGaAs Bragg reflection waveguides," Opt. Lett. **34**, 3656–3658 (2009).
3. J. B. Han, P. Abolghasem, D. Kang, B. J. Bijlani, and A. S. Helmy, "Difference-frequency generation in AlGaAs Bragg reflection waveguides," Opt. Lett. **35**, 2334–2336 (2010).
4. B. J. Bijlani and A. S. Helmy, "Bragg reflection waveguide diode lasers," Opt. Lett. **34**, 3734–3736 (2009).
5. C. Tong, B. J. Bijlani, S. Alali, and A. S. Helmy, "Characteristics of edge-emitting Bragg reflection waveguide lasers," IEEE J. Quantum Electron. **46**, 1605–1610 (2010).
6. A. S. Helmy, B. J. Bijlani, and P. Abolghasem, "Phase matching in monolithic Bragg reflection waveguides," Opt. Lett. **32**, 2399–2401 (2007).
7. B. Bijlani, P. Abolghasem, and A. S. Helmy, "Second harmonic generation in ridge Bragg reflection waveguides," Appl. Phys. Lett. **92**, 101124 (2008).
8. P. Abolghasem, J. Han, D. P. Kang, B. J. Bijlani, and A. S. Helmy, "Monolithic photonics using second-order optical nonlinearities in multi-layer core Bragg reflection waveguides," IEEE J. Sel. Top. Quantum Electron. **18**, 812–825 (2011).
9. T. Tamir and S. T. Peng, "Analysis and design of grating couplers," Appl. Phys. **14**, 235–254 (1977).
10. R. L. Roncone, L. F. Li, K. A. Bates, J. J. Burke, L. Weisenbach, and B. J. J. Zelinski, "Design and fabrication of a single leakage-channel grating coupler," Appl. Opt. **32**, 4522–4528 (1993).
11. D. Taillaert, W. Bogaerts, P. Bienstman, T. F. Krauss, P. Van Daele, I. Moerman, S. Verstuyft, K. De Mesel, and R. Baets, "An out-of-plane grating coupler for efficient butt-coupling between compact planar waveguides and single-mode fibers," IEEE J. Quantum Electron. **38**, 949–955 (2002).
12. J. Li and K. S. Chiang, "Light guidance in a photonic bandgap slab waveguide consisting of two different Bragg reflectors," Opt. Commun. **281**, 5797–5803 (2008).
13. Y. Li, Y. Xi, X. Li, and W. P. Huang, "A single-mode laser based on asymmetric Bragg reflection waveguides," Opt. Express **17**, 11179–11186 (2009).
14. R. Das and K. Thyagarajan, "Anomalous behaviour in a Bragg reflection waveguide," Opt. Commun. **273**, 84–88 (2007).
15. R. Das and K. Thyagarajan, "Broadband parametric amplification in Bragg reflection waveguide," J. Mod. Opt. **55**, 273–279 (2008).
16. P. Yeh, A. Yariv, and E. Marom, "Theory of Bragg fiber," J. Opt. Soc. Am. **68**, 1196–1201 (1978).
17. S. Gehrsitz, F. K. Reinhart, C. Gourgon, N. Herres, A. Vonlanthen, and H. Sigg, "The refractive index of $Al_xGa_{1-x}As$ below the band gap: accurate determination and empirical modeling," Appl. Phys. **87**, 7825–7837 (2000).
18. P. Abolghasem, J. Han, B. J. Bijlani, and A. S. Helmy, "Type-0 second order nonlinear interaction in monolithic waveguides of isotropic semiconductors," Opt. Express **18**, 12681–12689 (2010).
19. S. V. Zhukovsky, D. Kang, P. Abolghasem, L. G. Helt, J. E. Sipe, and A. S. Helmy, "Proposal for on-chip generation and control of photon hyperentanglement," Opt. Lett. **36**, 3548–3550 (2011).
20. G. I. Stegeman, A. Villeneuve, J. Kang, J. S. Aitchison, C. N. Ironside, K. Alhemyari, C. C. Yang, C. H. Lin, H. H. Lin, G. T. Kennedy, R. S. Grant, and W. Sibbett, "AlGaAs below half bandgap—the silicon of nonlinear-optical materials," Int. J. Nonlin. Opt. Phys. **1994**, 347–371 (1994).
21. E. Anemogianni and E. N. Glytsis, "Multilayer waveguides: efficient numerical analysis of general structures," IEEE J. Lightwave Technol. **10**, 1344–1351 (1992).
22. P. Abolghasem, M. Hendrych, X. Shi, J. P. Torres, and A. S. Helmy, "Bandwidth control of paired photons generated in monolithic Bragg reflection waveguides," Opt. Lett. **34**, 2000–2002 (2009).